Check for updates

ANNUAL ISSUE

Influence of tin doping on the liquefied petroleum gas and humidity sensing properties of NiO nanoparticles

Priya Gupta[1,a)] iD **, Kuldeep Kumar[3], Syed Hasan Saeed[1], Narendra Kumar Pandey[2], Vernica Verma[2], Peramjeet Singh[2], Bal Chandra Yadav[3]**

[1] Department of Electronics and Communication Engineering, Integral University, Lucknow, U.P. 226026, India
[2] Sensors and Materials Research Laboratory, Department of Physics, University of Lucknow, Lucknow, U.P. 226007, India
[3] Nanomaterials and Sensors Research Laboratory, Department of Physics, Babasaheb Bhimrao Ambedkar University, Lucknow, U.P. 226025, India
a) Address all correspondence to this author. e-mail: gupta101192@gmail.com

This research deals with study of enhanced liquefied petroleum gas (LPG) and humidity sensing properties of Sn-doped NiO pellets synthesized by chemical precipitation route. XRD, FTIR, SEM, and UV–Vis studies were employed to understand the effect of Sn doping on the structural, morphological, and optical properties of the NiO nanoparticles. XRD results revealed that doping of tin in NiO had a significant impact on the crystallite size, peak intensity, strain, lattice parameter, etc. The calculated crystallite size of pure and 3 mol% doped NiO was 33.2 nm and 13.3 nm, respectively. SEM micrographs revealed that the structure of the samples was irregular spheres and non-homogeneous. The dependence of LPG sensing properties on the structural and surface morphological properties has also been studied. The maximum response of 30.46% to 2.0 vol% of LPG was observed at room temperature (300 K). The same sample also shows high humidity sensing response of 87.11% towards 90% RH.
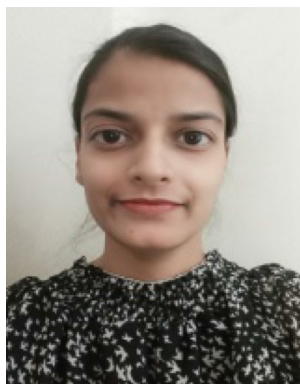
Priya Gupta received a Bachelor of Engineering in Electronics & Communication Engineering from Integral University, Lucknow, India in 2012 and a Master of Engineering in Communication Engineering from Madan Mohan Malaviya University of Technology, Gorakhpur, India in 2014. She received her PhD degree at Integral University, Lucknow, India in collaboration with the Sensor and Actuator Lab, Department of Physics, University of Lucknow. Her areas of interest include humidity and gas sensing, nanotechnology, and communication engineering.

Priya Gupta

Introduction

The development of sensitive and selective sensor is of primarily importance for safety purposes in many fields such as homes, hotels, industries, kitchens, etc. A reliable and sensitive liquefied petroleum gas (LPG) sensor prevents accidents by presenting an alarm for the leakage of LPG and, thus, increases safety. Similarly, humidity sensors have found many uses in life science, industry, and other applications where humidity measurement has improved quality and comfort. Therefore, the development of new sensing materials and technologies has motivated enormous research activities across the world [1, 2]. Most of the authors reported sensing properties of sensors working at high operating temperatures, such as 250 °C or above, which is undemanding for commercialization of the sensor [3, 4]. Therefore, nowadays,

the researchers are giving more attention on the development of a highly sensitive room-operated sensor that gives small response and recovery times along with high stability [5–7]. The sensing mechanism is a surface-controlled phenomenon which depends on the nanostructures of sensing devices. Hence, the correlation between structure and sensing properties is an active area of sensor research and development by the researchers [8, 9].

Semiconductor metal oxide-based sensors have attracted considerable interest owing to their easy production, low cost, compact size, and simple sensing principle [10, 11]. The performance of metal oxide-based sensors is significantly influenced by the structure and morphology of sensing materials. Thus, sensors based on nanomaterials are developed by the researchers to improve sensing properties such as sensitivity, selectivity, and response/recovery speed. Several metal oxides such as ZnO, SnO_2, TiO_2, Fe_2O_3, WO_3, and NiO have been employed for sensing applications [12, 13]. Among these metal oxides, Nickel oxide has been studied as an attracting material for various applications such as in the fabrication of sensors, piezoelectric devices, fuel cells, etc. The worldwide researchers have been trying to fabricate gas and humidity sensor having more sensitivity, long-term stability, and small response and recovery times. There are various literatures reporting the NiO-based gas sensors like Cr-doped NiO [14], NiO/In_2O_3 [15], TiO_2 nanorods decorated with NiO nanoparticles [16], Ce-doped NiO nanoparticles [17], and NiO-based thin films with Pt surface modifications [18] used for the detection of different gases like xylene, methanol, acetone, nitrogen dioxide, and hydrogen, respectively. But a little attention was given to investigate the LPG as well as humidity sensing of NiO structures. Table 1 shows the comparison of different specifications like sensor response, gas

concentration, and operating temperature of the present work with previously reported metal oxide-based materials for LPG and humidity sensing.

In this work, we have reported a simple and cost-effective chemical precipitation method to synthesize tin-doped Nickel Oxide nanoparticles and study the impact of tin doping in the enhancement of LPG and humidity sensing properties along with its structural, morphological, and optical properties. SN0, SN1, SN2, and SN3 represents 0 mol%, 1 mol%, 2 mol%, and 3 mol% Sn-doped NiO samples. Among all the prepared samples, NiO doped with 3 mol% Sn shows maximum sensing response of 30.46% for 2.0 vol% LPG and 87.11% for 90% RH at room temperature. The utilization of nanostructured Sn-doped NiO towards LPG and humidity sensing at room temperature is a relatively new approach as very few authors have reported about the sensing properties of NiO and as per our survey, none of the authors reported the effect of tin doping on the LPG sensing and humidity sensing properties of NiO. The experimental results indicate that the synthesized Sn-doped nickel oxide is a promising material for the designing of both LPG and humidity sensor.

Results and discussions

X-ray diffraction (XRD) analysis

The XRD pattern was obtained in the 2θ range from 35° to 70°. Figure 1a shows the X-ray diffraction patterns of pure and Sn-doped NiO powder samples. The observed diffraction peaks can be indexed to a standard cubic NiO structure with no visible defects or impurity peaks. Since ionic radii of Ni^{2+} and Sn^{2+} are almost similar, it is easily incorporated into the Ni^{2+} when the

TABLE 1: Response of metal oxide-based sensors towards LPG and humidity.

| Material	Method	Target gases	Gas Conc. (ppm)	Operating Temp. (°C)	Resp.	Year/Refs.
ZnO/NiO hetero-structures Thick film	Chemical precipitation	LPG	50 ppm	200	30	2019 [19]
NiO thin film	SILAR	LPG	5000 ppm 100 ppm	180 180	72% 10%	2017 [20]
NiO thick film	Hydrothermal	LPG	100 ppm	150	6	2012 [21]
Ni0.99Co0.01Mn0.02Fe1.98O4-δ	Self-combustion method	LPG	–	190	0.4%	2005 [22]
HST doped NiO	Green method	Humidity	–	Room temp	62,500	2014 [23]
Manganese-doped nickel oxide	Immersion method	Humidity	–	Room temp	270	2019 [24]
Zn-doped NiO	Chemical precipitation method	LPG	2.0 vol%	Room temp	5.33%	2021 [25]
Nickel oxide (NiO) nanowall network films	Sonicated sol–gel immersion	Humidity	–	Room temp	1.80×10^3	2018 [26]
Cu-doped ZnO	Spin coating	Humidity	–	Room temp	20.68 MΩ/%RH	2016 [27]
Ruthenated Tin Oxide	Pellets	LPG	1000 ppm	300	320	1999 [28]
Sn-doped NiO	Chemical precipitation method	LPG	2.0 vol%	Room temp	30.46%	This work
Sn-doped NiO	Chemical precipitation method	Humidity	90% RH	Room temp	87.11%	This work
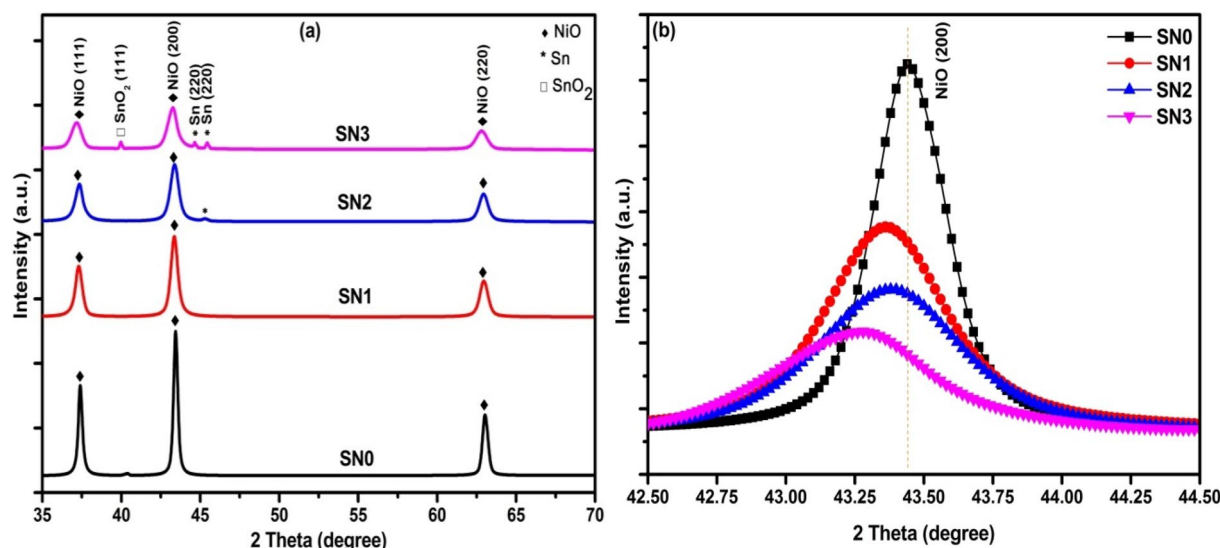
Figure 1: (a) XRD patterns and (b) Magnified view of (200) peak of the pure and tin-doped nickel oxide nanoparticles.

doping amount is small, excessive doping ion makes it unstable. The reduced crystallinity may be due to the fact that Sn favors the creation of more nucleation sites which, in turn, inhibit the growth of crystal grains. However, all the peaks have a slight shift toward lower angles with increasing Sn concentration compared with pure NiO, which suggest the successful incorporation of dopant ions in the NiO host structure. The larger ionic radius of the tin ion (0.071 nm) compared with the nickel ion (0.069 nm) tends to increase the size of the lattice in doped NiO. In '2 mol% and 3 mol% Sn–NiO', several weak additional diffraction peaks appeared, which are assigned to the secondary phase of SnO_2 due to an easy oxidization of Sn to SnO_2 during high-temperature heat treatment in open air. The appearance of SnO_2 peaks indicates the solubility limitation of the dopant in the host NiO. Along with the secondary phase of SnO_2, some metallic Sn phase peaks are also observed. The new and very small peaks are analyzed to be Sn metal impurity phase (JCPDS 04-0673) and SnO_2 (JCPDS-14-1445) which may have appeared due to the clustering of tin either in the grain boundary or interstitial position. As seen from the XRD patterns, Sn, SnO_2, and NiO reflections were determined but NiO peak with the highest intensity was found at $2\theta = 43.45°$. The intensity of the diffracted peaks and crystallite size showed

decrease with increase in Sn-doping level. From Fig. 1b, it was clear that the intensity at lower doping level (1 mol%) is maximum whereas the intensity for the higher doping level (3 mol%) is minimum, which may be due to impurities that oppose the growth of NiO. The same decrease in the intensity of the diffracted peaks with the increase of doping level was also reported in Fe-doped SnO_2 synthesized by sol–gel [29].

The crystallite sizes were calculated by the Scherrer equation [30]:

$$D = \frac{K\lambda}{\beta \cos \theta} \qquad (1)$$

where K is a constant, λ is the diffraction wavelength of CuK_α, β is the full width at half maximum (FWHM) in radians, and θ is the diffracted angle. Calculated crystallite size values vary between ~ 13 and ~ 33 nm. The lattice parameter (a) and unit cell volume (V) showed increase from 4.164 to 4.179 Å, and 72.199 Å to 72.982 Å, respectively, with the increase of Sn-doping level from 0 to 3 mol%. Dislocation density (δ) and internal strain (ε) are calculated by the following equations:

$$\delta = \frac{1}{D^2}, \qquad (2)$$

TABLE 2: Summary of parameters obtained from structural analysis of the pure and Sn-doped NiO samples.

Sample	2θ (200)	D Nm	FWHM (deg)	Lattice parameter($a=b=c$) (Å)	Inter-planner distance (d) (Å)	Dislocation density $\delta \times 10^{16}$ (line/m^2)	Unit cell volume ($V=a^3$) (Å)^3	Internal strain ($\varepsilon \times 10^{-3}$)
SN0	43.423	33.2	0.269	4.164	2.082	0.091	72.199	1.09
SN1	43.332	18.2	0.491	4.173	2.086	0.302	72.668	1.99
SN2	43.351	14.7	0.606	4.171	2.085	0.462	72.564	2.45
SN3	43.262	13.3	0.672	4.179	2.089	0.565	72.982	2.72

$$\varepsilon = \frac{\beta \cos\theta}{4}, \tag{3}$$

The FWHM of the Sn-doped NiO powders showed an increase from 0.269° to 0.672° with increase of Sn-doping level from 0

to 3 mol%. A summary of Sn-doping levels (mol%), full width at half maximum (FWHM), 2θ (2 0 0) from XRD, crystallite size (D), lattice parameters ($a = b = c$), inter-planner distance (d), dislocation density (δ), internal strain (ε), and unit cell volume (V) is given in Table 2.
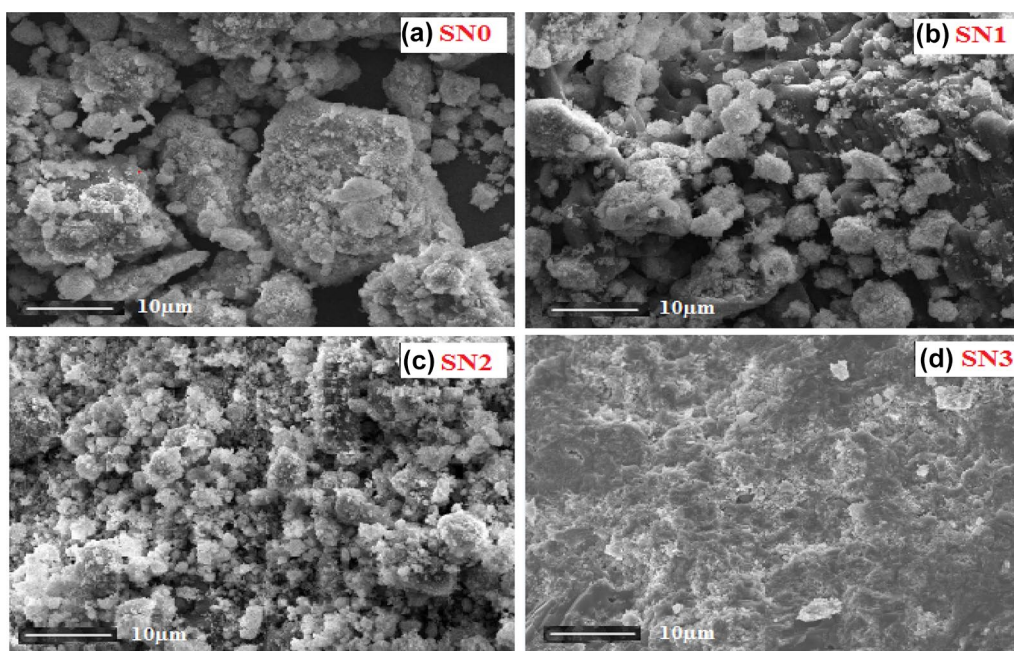
Figure 2: SEM micrographs of (a) pure and (b–d) Sn-doped NiO nanoparticles.
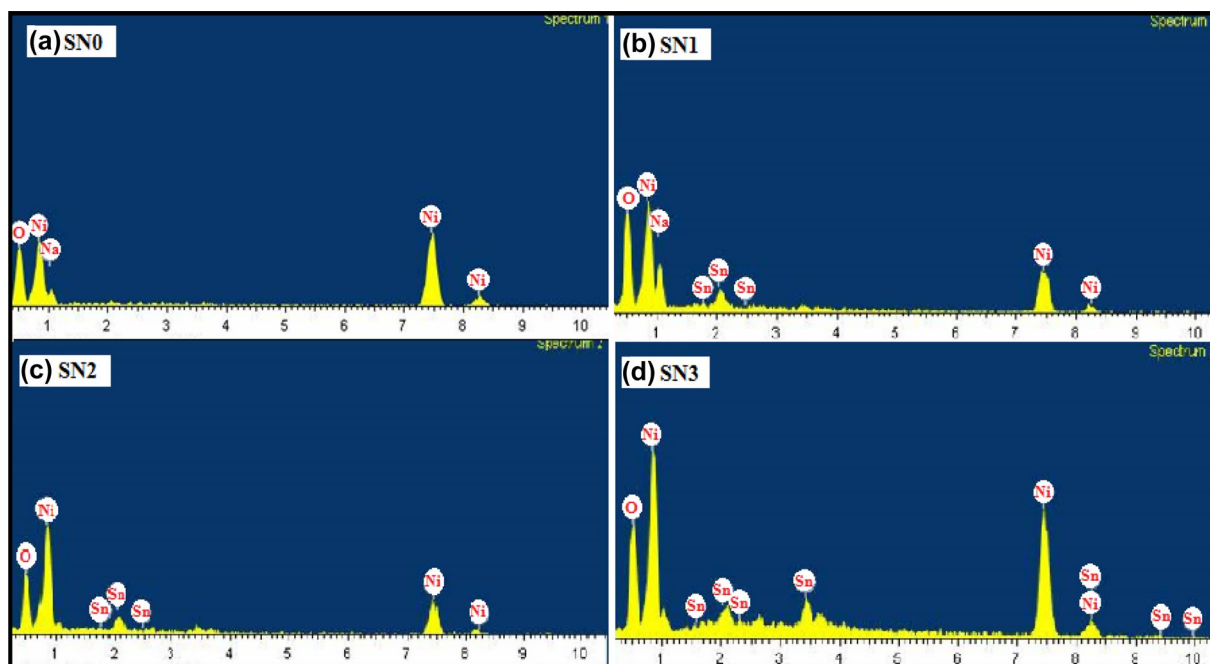
Figure 3: EDS patterns of (a) pure and (b–d) tin-doped nickel oxide samples.

Scanning electron microscopy (SEM) analysis

Surface morphology investigated through SEM reveals that the size of the particle decreases with increase in tin concentration from 0 to 3 mol% in NiO. In addition to this, specific surface area of the crystalline particle increases from 27.09 to 67.63 m^2/gm as we increase the concentration from 0 to 3 mol%. The specific surface area (S) is determined using Eq. (4) [31]:

$$S = \frac{6}{d \times D}, \tag{4}$$

where d is the bulk density of NiO (6.67gm/cm^3) and D is the average crystallite size. The number 6 is a shape factor. All samples have irregular and non-homogeneous spherical structure. Figure 2a-d represents SEM images of pure and Sn-doped NiO nanoparticles.

Energy dispersive X-ray spectroscopy (EDS) analysis

The elemental conformation of pure and Sn-doped NiO nanoparticles was investigated by energy-dispersive X-ray spectroscopy shown in Fig. 3. There were no impurities found in the as-produced Sn-doped NiO nanoparticles while there is a small percentage of Na impurity present in pure NiO. As the amount of impurity present in this sample is very small compared to the percentage of main elements, so we can assume that it will not

affect the characteristics of sample. Apparently, all three types of elements Sn, Ni, and O were detected in Sn-doped NiO nanoparticles (Table 1, Supplementary data). Likewise, the intensity of Sn peak was much smaller than that of Ni and O peaks, signifying that the concentration of Sn was lower as compared to Ni and O in Sn-doped NiO.

UV–Vis spectroscopy

To study the influence of Sn doping on the optical band gap, absorbance spectra were recorded for all Sn-doped NiO powder samples. Figure 4a shows the optical absorbance spectra of pure NiO and Sn-doped NiO powder samples at different Sn-doping levels. The pure NiO powder exhibited a maximum absorbance at a wavelength of 291 nm. When Sn-doping level has increased, the absorbance of the samples showed a decrease. It may be due to the dopant impurities which could decrease absorbance. The optical band gap (E_g) for a highly degenerated semiconducting oxide can be determined from the absorption coefficient (α) and photon energy (hυ) using the following relation [32]:

$$\alpha h\upsilon = A\left(E_g - h\upsilon\right)^{1/2}. \tag{5}$$

The optical bang gap (E_g) was calculated by plotting $(\alpha h\upsilon)^2$ versus the photon energy ($h\upsilon$) and by extrapolating the linear region of the plots to zero absorption ($\alpha = 0$) (Figure 4b). As observed from the Tauc plot, the optical band gap of the powder samples decreased from 4.04 to 3.97 eV when the Sn-doping level was increased from 0 to 3 mol%. Similar results were also reported in Ni-doped SnO$_2$ nanoparticles by Ahmed et al. [33]. A decrease in optical band gap with doping level has been explained by many groups who suggested the alloying effect in the host compound with some impurity phases [34].
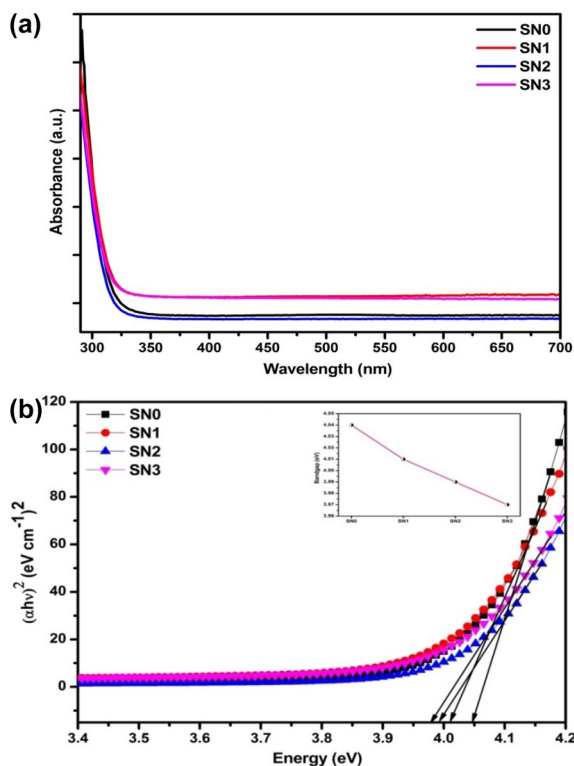

Figure 4: (a) UV–Vis spectra and (b) plot of $(\alpha h\upsilon)^2$ versus ($h\upsilon$) for pure and tin-doped nickel oxide.

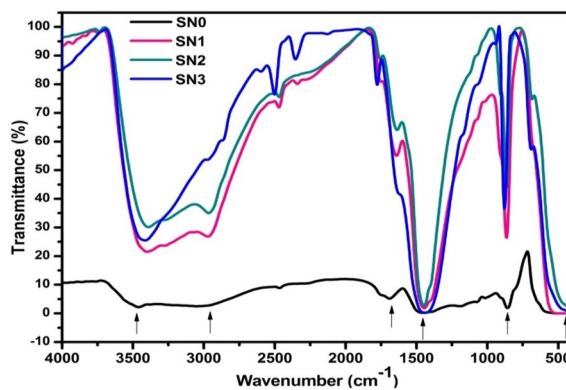**Figure 5:** FTIR spectra of pure and Sn-doped NiO samples.
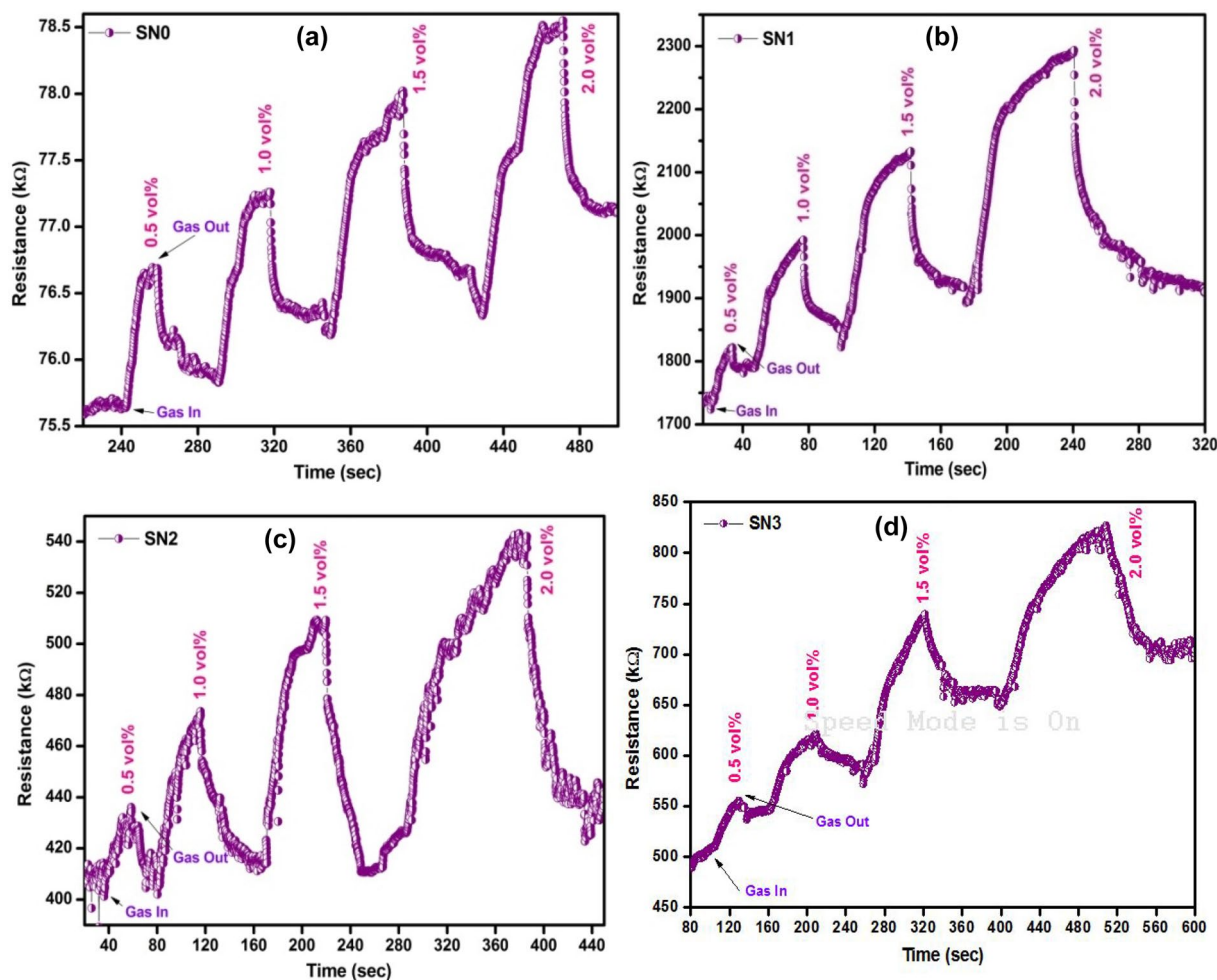
Figure 6: LPG sensing characteristics of (a) pure and (b–d) Sn-doped NiO samples.
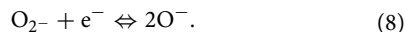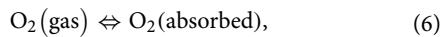
FTIR analysis

Figure 5 depicts the measured Fourier Transform Infrared (FTIR) spectra of pure and Sn-doped NiO (4000-400 cm^{-1}). The broad absorption band centered at about 3460.4 cm^{-1} is originated from the O–H stretching vibration, and the band in between 1690 and 1640 cm^{-1} is assigned to H–O–H bending vibrations which suggest the presence of physisorbed and coordinated water linked to precursor when FTIR sample disks were prepared in an open air. The presence of C–O in the precursor is confirmed by the band around 857.4 cm^{-1}, and the band at 1447.7 cm^{-1} is primarily due to the bending vibration of ionic CO_3^{2-} which shows the adsorption of CO_2 present in the atmosphere on the surface of NiO. The vibration band of CH_2 that occurs at 3052.2 cm^{-1} indicates the presence of residual organic compounds. The spectrum of the Sn-doped NiO samples clearly shows the Ni–O absorption band near ~ 450 cm^{-1} and is due to stretching NiO mode. The broadness of the adsorption band

indicates that the NiO powders are nanocrystal. We further observe that FTIR spectra do not show any impurity or other precursor characteristics peaks.

LPG sensing study

Figure 6a–d shows the gas sensing response of the pure and three Sn-doped NiO samples when exposed to 0.5–2.0 vol% LPG at room temperature. LPG sensing response of the sample mainly depends on its surface morphology. When sample is exposed to the LPG, its electrical resistance varies due to the interaction of material with gas which leads to the transfer of electrons between gas and sensing material. It is known that only a certain amount of oxygen from air is adsorbed on the surface of NiO. When sample surface interacts with the atmospheric oxygen, ionic species such as O_2^- or O^- get formed due to the transfer of electrons from the conduction band to adsorbed

oxygen atoms. The reaction kinematics may be explained by the following reactions:

$$O_2(gas) \Leftrightarrow O_2(absorbed),\qquad(6)$$

$$O_2(absorbed) + e^- \Leftrightarrow O_2^-,\qquad(7)$$

$$O_{2-} + e^- \Leftrightarrow 2O^-.\qquad(8)$$

The electron transfer from the conduction band to the chemisorbed oxygen results in decrease in the electron concentration, thus, decreases the resistance of NiO pellets. When NiO further interacts with the reducing gas like LPG, the LPG molecules react with the chemisorbed oxygen thereby releasing the electrons back to the conduction band. As a result, resistance of the NiO pellet increases. The overall reaction of LPG with the chemisorbed oxygen can be explained as follows:

$$C_nH_{2n+2} + 2O^- \rightarrow H_2O + C_nH_{2n}O^- + e^-.\qquad(9)$$
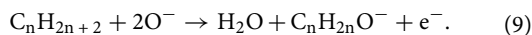
The response of the sample to test LPG at room temperature was calculated using Eq. (10) [25]:

$$S_G(\%) = \frac{R_g - R_o}{R_o} \times 100\%,\qquad(10)$$

where R_o and R_g indicate the resistance of the sensor measured in the dry air atmosphere and gas atmosphere, respectively. It is observed that 3 mol% tin-doped nickel oxide pellet has higher sensor response which increases with an increase in concentration of LPG. This is due to the presence of larger active surface area with possible reaction sites on the sample surface. The variation of sensor response, recovery time, and response time with LPG concentration is given in Table 2, Supplementary data.

The dependency of the sensor response of the synthesized NiO-based samples on the LPG concentration from 0.5 to 2.0 vol% is shown in Figure 7a. It is observed form the results that the sensor response increases linearly with increase in LPG concentration. The linear relation between sensor response
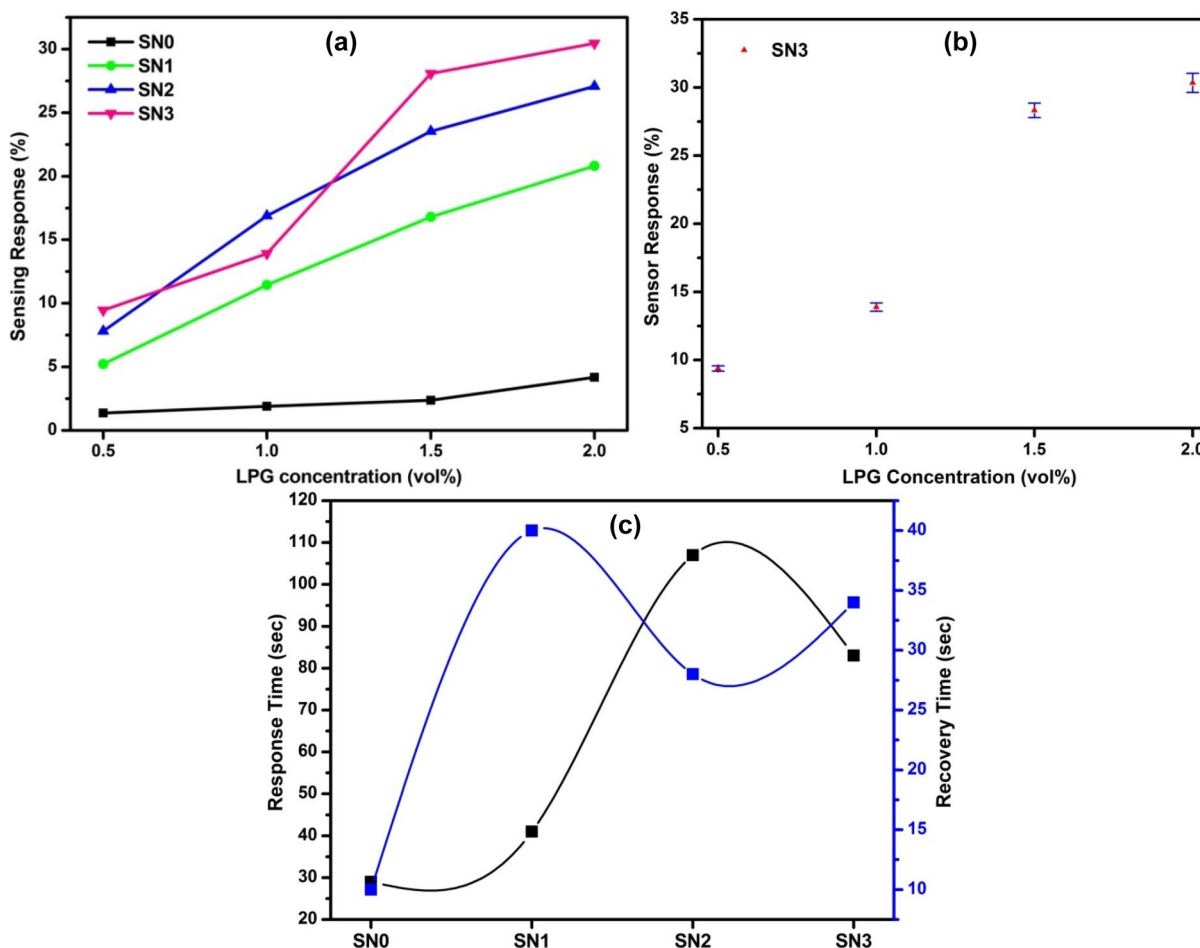

Figure 7: (a) Variation of sensing response with LPG concentration for pure and Sn-doped samples. (b) The error bars represent the standard deviation ($n = 4$) for SN3 sample. **c** Variation of response and recovery time with doping percentage at exposure of 2.0 vol% LPG.
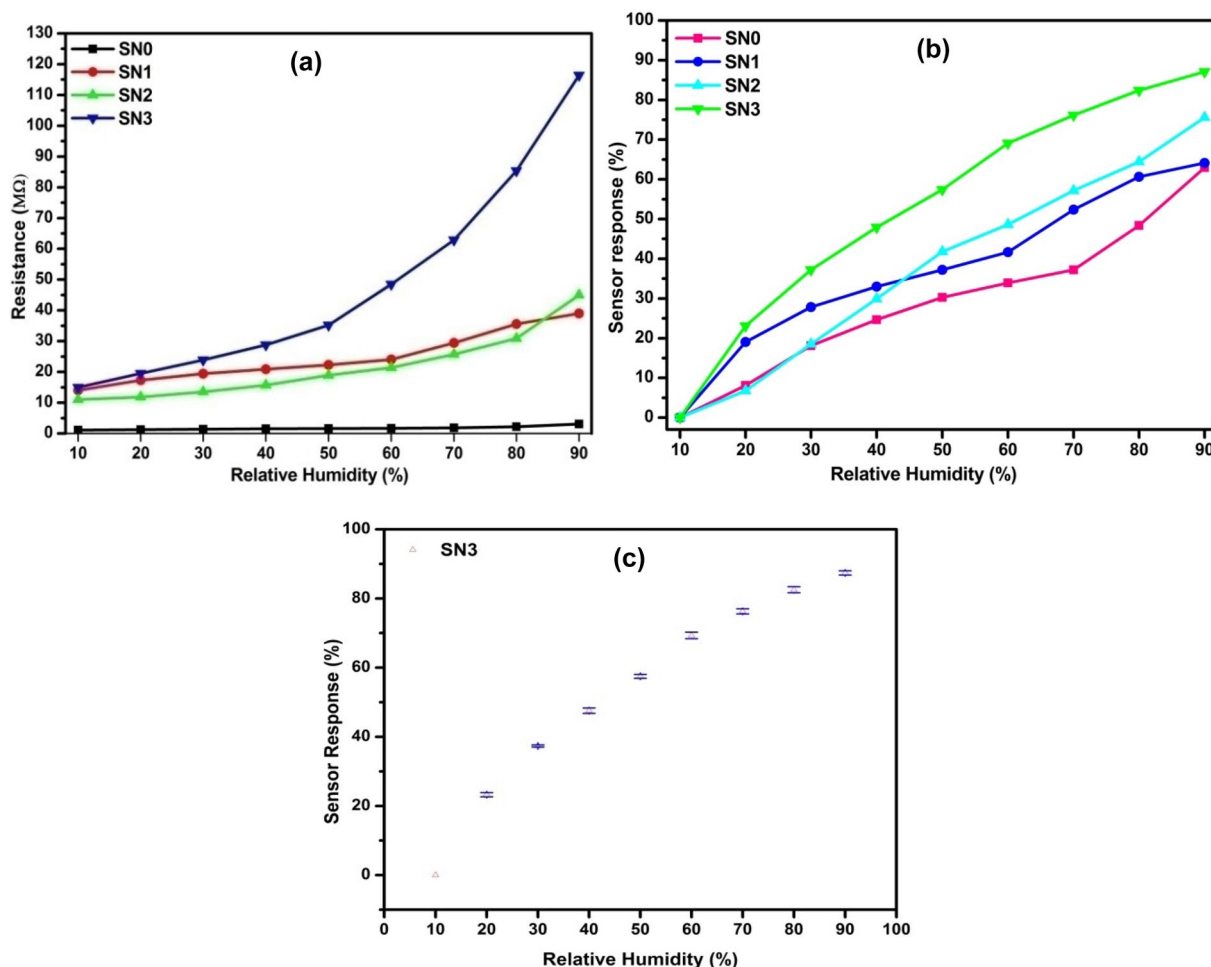
Figure 8: Variation of (a) resistance, (b) sensor response, and (c) error bars for SN3 sample with relative humidity.

and the LPG concentration may be ascribed due to the sufficient number of sensing sites available on the pellet surface. Figure 7b is the plot of the response of SN3 sample as a function of LPG concentration with error bars, representing the standard deviation ($n = 4$), are relatively small suggesting a high manufacturing yield. The response and recovery time is also an important parameter used for characterizing a sensor. The variation of response and recovery times with different concentration of LPG at room temperature is given in Figure 7c. It is observed that response and recovery time shows random variation with doping percentage. The response/recovery time of pure NiO is 29/10 s which increases with 3 mol% Sn doping in NiO to 83/34 s for 2.0 vol% LPG.

Humidity sensing analysis

Humidity sensor responses of the prepared samples at room temperature with various RH (relative humidity) levels with error bars are shown in Figure 8a–c. During the adsorption process (10–90% RH), resistance increased steadily with increasing RH. On the

other hand, during the desorption process (90–10% RH), resistance rapidly dropped until the signal recovers back to its initial current value. The sensing response of pure and doped NiO-based humidity sensors was estimated by using resistance data obtained from the response curve by using the following relation [20]:

$$S_H(\%) = \frac{R_{10\%} - R_x}{R_x}, \tag{11}$$

where S_H is sensitivity, $R_{10\%}$ is the resistance of the sensor under exposure to the 10% RH humidity level, and R_x is the resistance of the sensor at the x% RH humidity level. The nano-scale structure in NiO is very important in humidity detection due to larger surface-to-volume ratio and chemically reactive surface. The nanostructured surface of NiO consists of high concentrations of oxygen vacancies, which provides highly active sites for water molecules adsorption. High active surface area is one of key factors that determine the high performance of a humidity sensor. The basic mechanism of a humidity sensor involves water molecules getting attached to the NiO surface following the Grotthuss chain reaction:

$$2H_2O \rightarrow H_3O^+ + OH^- \atop H_3O^+ \rightarrow H_2O + H^+ \Biggr\} . \qquad (12)$$
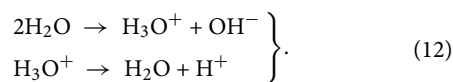
The source of charge carriers is from the protonic transfer (H^+) among hydronium ions (H_3O^+) which is known by the term proton hopping. A higher surface area offers more surface reactions between the sensing element and water molecules leading to a greater number of carriers. The values of sensitivity for 0 mol%, 1 mol%, 2 mol%, and 3 mol% Sn-doped NiO-based humidity sensors for 90% RH were calculated to be 62.95%, 64.10%, 75.55%, and 87.11%, respectively. All doped samples show an improved performance in humidity sensing compared to the pure NiO sample. Zhu et al. reported that the doping process can increase the concentration of oxygen vacancies when the doping elements substituted the ZnO lattice which improved the performance of humidity sensor [35].

Response and recovery times are among the most imperative elements for evaluating the performance of humidity sensors. It is noted that the time taken by a sensor to achieve 90% of the total resistance change is defined as the response time in the case of adsorption or the recovery time in the case of desorption. The response/recovery times of the pure and 3 mol% Sn-doped NiO were measured to be 82/60 and 43/38 s, respectively, at 90% RH.
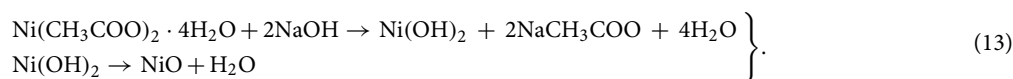
Response and recovery behavior of sensor is dependent on large surface-to-volume ratio, where it helps increase the adsorption of water molecules on the sensing element surface.

Conclusion

Conclusively, the present chapter reports the synthesis of pure and Sn-doped NiO powder by chemical precipitation route. The resulting powders were characterized for its structural, morphological and optical properties along with its LPG and humidity sensing properties. Structural characterization of the samples revealed cubic NiO structure similar to NaCl. SEM images confirm that nanocrystals have irregular and non-homogeneous spherical structure. The average crystalline size decreases from 33.3 to 13.3 nm as the doping concentration has increased which increases the active surface area for the adsorption of LPG and water molecules. As a result, NiO sample doped with 3 mol% Sn is having highest sensing response of 30.46% towards 2.0 vol% LPG and 87.11% towards 90% RH.

Materials and methods

Preparation of samples

The reagents used for the synthesis of sample were Nickel Acetate Tetrahydrate [M = 248.84, Ni $(CH_3COO)_2 \cdot 4H_2O$], Sodium Hydroxide [M = 40, NaOH], Ethanol [M = 46.07, C_2H_4O], Stannous Chloride dihydrate [M = 225.63, $SnCl_2.2H_2O$], and distilled water. Pure and Sn-doped NiO powders at 1, 2, and 3 mol% of Sn were prepared by a standard chemical precipitation method. First, we have dissolved 12.44 g of nickel acetate tetrahydrate in 200 ml distilled water to prepare 0.5 M solution and stirred it vigorously for 2 h. Add NaOH pellets to this solution during the stirring and further stir the solution for 4 h at 40 °C to maintain pH in the range of 8 to 12. The resultant light-green solution was filtered after leaving it overnight and then washed with distilled water and ethanol for 4–5 times and dried it at 100 °C for 2 h. After cooling at room temperature, it was grounded finely in mortar and pestle. The obtained NiO powder was then annealed for 4 h at 500 °C. The Sn-doped nickel oxide was also prepared using the similar steps. The only difference was the addition of 1, 2 and 3 mol% stannous chloride dihydrate ($SnCl_2 \cdot 2H_2O$) in the prepared nickel acetate solution. Therefore, high-purity NiO and Sn-doped NiO nano-powder can be obtained successfully by this synthesis route. Main reactions occur during the experimental procedure can be written briefly as follows:

$$Ni(CH_3COO)_2 \cdot 4H_2O + 2NaOH \rightarrow Ni(OH)_2 + 2NaCH_3COO + 4H_2O \atop Ni(OH)_2 \rightarrow NiO + H_2O \Biggr\} . \qquad (13)$$

The obtained powder samples after annealing were pressed into the shape of pellet in a hydraulic machine by applying uniaxial pressure of 7 ton at room temperature. The prepared disk shape pellet samples were having a thickness of 2 mm and diameter of 12 mm. Further, all the prepared pellets were annealed for 2 h at 500 °C in an electric muffle furnace with temperature control to provide physical stability.

Characterizations

The synthesized material was characterized by X-ray diffractometer (Ultima IV model (Rigaku, Japan)) to study its structural properties. The X-ray diffraction (XRD) data were recorded using CuK_α radiation having a wavelength (λ) of 1.5406 Å. The surface morphologies of the sensing films were observed by scanning electron microscope (Leo-430, Cambridge, England). Optical characterizations were done by UV–Visible (UV–Vis) absorption spectrophotometer (Evolution 201) in UV and visible region and with a Fourier transform infrared (FTIR) spectrometer (Nicole TM 6700).

Gas sensing and humidity sensing setups

The LPG and humidity sensing measurement setup has been designed in our laboratory and described in our previous published paper [36, 37]. The gas sensing property of the prepared NiO samples was evaluated using a specially designed measurement. The closed gas chamber is having the holder to put pellet upon it and is connected to a Keithley electrometer to record the variations in pellet resistance with LPG concentration. The gas chamber was maintained at room temperature during the experiment and the gas concentration was varied from 0.5 to 2.0 vol% by step size of 0.5 vol % using a mass flow meter with a controller used to control the concentration of gas inside the chamber. The pellet sample was placed for 1 h in the vacuum chamber before the exposure of LPG to remove contaminations from the pellet surface.

For studying the humidity sensing properties of the prepared samples, a specially designed humidity control chamber with humidity variation from 10 to 90% RH. A standard hygrometer (± 1%RH, digital) was placed inside the humidity chamber for the purpose of calibration. Variation in a resistance is recorded by a multifunctional digital multimeter (± 0.001 $M\Omega$.VC-9808) with respect to change in percentage relative humidity. The potassium sulfate (K_2SO_4) solution is used as a humidifier and potassium hydroxide (KOH) pellets are used as a dehumidifier. Two thin copper plates are used for making the electrical contacts on the surfaces of the pellets to measure its resistance. The copper sheets are used in such a way to cover the two opposite cross-sectional areas of the pellet.

Acknowledgments

Data availability

All data generated or analyzed during this study are included in this published article and its supplementary information files.

Declarations

Conflict of interest The authors declare that they have no known competing financial interests or personal relationships that could have appeared to influence the work reported in this paper.

Supplementary Information

The online version contains supplementary material available at https://doi.org/10.1557/s43578-021-00418-9.

Open Access

References

1. L. Satyanarayana, K.M. Reddy, S.V. Manorama, Mater. Chem. Phys. **82**, 21–26 (2003)
2. B.C. Yadav, S. Singh, A. Yadav, Appl. Surf. Sci. **257**, 1960–1966 (2011)
3. V.R. Shinde, T.P. Gujar, C.D. Lokhande, R.S. Mane, S.H. Han, Sens. Actuators B **123**, 882–887 (2007)
4. R.R. Salunkhe, D.S. Dhawale, U.M. Patil, C.D. Lokhande, Sens. Actuators B **136**, 39–44 (2009)
5. R.B. Kamble, V.L. Mathe, Sens. Actuators B **131**, 205–209 (2008)
6. B.C. Yadav, A. Yadav, T. Shukla, S. Singh, Sens. Lett. **7**, 1119–1123 (2009)
7. A. Singh, S. Singh, B.D. Joshi, A. Shukla, B.C. Yadav, P. Tandon, Mater. Sci. Semicond. Process **27**, 934–950 (2014)
8. R.C. Pawar, J.S. Shaikh, S.S. Suryavanshi, P.S. Patil, Curr. Appl. Phys. **12**, 778–783 (2012)
9. L. Zhu, W. Zeng, Y. Li, J. Yang, Physica E **106**, 170–175 (2019)
10. A.A. Tomchenko, G.P. Harmer, B.T. Marquis, J.W. Allen, Sens. Actuators B **93**, 126–134 (2003)
11. S.M. Kanan, Q.M. El-Kadri, I.A. Abu-Yousef, M.C. Kanan, Sensors **9**, 8158–8196 (2009)
12. S. Nasirian, H.M. Mooghaddam, Appl. Surf. Sci. **328**, 395–404 (2015)
13. S.S. Shendage, V.L. Patil, S.P. Patil, S.A. Vanalakar, J.L. Bhosale, J.H. Kim, P.S. Patil, J. Anal. Appl. Pyrol. **125**, 9–16 (2017)
14. C. Feng, X. Kou, X. Liao, Y. Feng, S.G. Lu, RSC Adv. **7**, 41105–41110 (2017)
15. H. Xuemei, S. Yukun, B. Bo, J. Nanomater. (2016). https://doi.org/10.1155/2016/7589028
16. P. Sunghoon, S.G. Joo, K. Hyejoon, C. Seungbok, L. Chongmu, J. Nanosci. Nanotechnol. **16**, 8589–8593 (2016)

17. S.R. Gawali, V.L. Patil, V.G. Deonikar, S.S. Patil, D.R. Patil, P.S. Patil, J. Pant, J. Phys. Chem. Solids **114**, 28–35 (2018). https://doi.org/10.1016/j.jpcs.2017.11.005

18. I. Hotovy, J. Huran, P. Siciliano, S. Capone, L. Spiess, V. Rehacek, Sens. Actuators B **221**, 1196–1201 (2004)

19. G. Singh, R.C. Singh, J. Mater. Sci.: Mater. Electron. **30**, 20010–20018 (2019)

20. S.U. Mutkule, S.T. Navale, V.V. Jadhav, S.B. Ambade, M. Naushad, J. Alloys Compd. **695**, 2008–2015 (2017)

21. D.V. Ahire, G.E. Patil, G.H. Jain, V.B. Gaikwad, in Sixth International Conference on Sensing Conferences (2012)

22. E. Rezlescu, N. Iftimie, P.D. Popa, N. Rezlescu, J. Phys. Conf. Ser. **15**, 51–54 (2005)

23. L.J. Kennedy, P. Magesan, J.J. Vijaya, M.J. Umapathy, U. Aruldoss, Mater. Sci. Eng. B **190**, 13–20 (2014)

24. N. Parimon, M.H. Mamat et al., in NanoMITe Annual Symposium and Nanotechnology Malaysia Annual Symposium (2019)

25. P. Gupta, N.K. Pandey, K. Kumar, B.C. Yadav, Sens. Actuators A **319**, 112484 (2021)

26. M.H. Mamat et al., J. Eng. Technol. **7**, 277–282 (2018)

27. S.K. Misra, N.K. Pandey, J. Mater. Res. **31**, 3214 (2016)

28. V.A. Chaudhary, I.S. Mulla, K. Vijayamohanan, J. Mater. Res. **14**, 185 (1999)

29. K. Nomura, C.A. Barrero, J. Sakuma, M. Takeda, Phys. Rev. B **75**, 184411 (2007)

30. A.L. Patterson, Phys. Rev. **56**(10), 978 (1939)

31. B.C. Yadav, S.R. Sabhajeet, R.K. Sonkar, J. Mater. Sci. Res. (2018). https://doi.org/10.29011/JMSR-108/100008

32. J. Tauc, *Amorphous and Liquid Semiconductors* (Plenum Press, New York, NY, 1974)

33. A.S. Ahmed, M.M. Shafeeq, M.L. Singla, S. Tabassum, A.H. Naqvi, A. Azam, J. Lumin. **131**(1), 1–6 (2011)

34. N. Barreau, J.C. Bernede, S. Marsillac, A. Mokrani, J. Cryst. Growth **235**(1–4), 439–449 (2002)

35. D. Zhu, T. Hu, Y. Zhao, W. Zang, L. Xing, X. Xue, Sens. Actuators B Chem. **213**, 382–389 (2015)

36. P. Gupta, K. Kumar, N.K. Pandey, B.C. Yadav, S.H. Saeed, Appl. Phys. A **127**, 289 (2021)

37. P. Gupta, S. Maurya, N.K. Pandey, V. Verma, J. Mater. Sci. Mater. Electron. **32**, 3529–3542 (2021)